ADVANCED FUNCTIONAL MATERIALS
www.afm-journal.de

www.MaterialsViews.com

# Strong Spin-Lattice Coupling Through Oxygen Octahedral Rotation in Divalent Europium Perovskites

*Hirofumi Akamatsu,* Yu Kumagai, Fumiyasu Oba, Koji Fujita, Katsuhisa Tanaka, and Isao Tanaka*

**First-principles calculations reveal that in divalent europium perovskites Eu$MO_3$ ($M$ = Ti, Zr, and Hf), antiferromagnetic superexchange interactions via $n$d states of the B-site $M$ cations ($n$ = 3, 4, and 5, respectively) are enhanced by rotations of the $MO_6$ octahedra. The octahedral rotations involved in a structural change from cubic $Pm\bar{3}m$ to orthorhombic $Pbnm$ structures not only reduce energy gaps between the Eu 4$f$ and $M$ $n$d bands but also point the $M$ $n$d orbitals at the Eu sites, leading to a significant overlap between the $M$ $n$d and Eu 4$f$ orbitals. These results reveal that the octahedral rotations are indispensable for antiferromagnetic ordering observed for $EuZrO_3$ and $EuHfO_3$, and put these perovskites into a class of materials exhibiting a novel type of strong coupling between their magnetism and octahedral rotations.**

## 1. Introduction

$ABO_3$ perovskite oxides often present structural distortions associated with rotations of the $BO_6$ octahedra, leading to lower symmetry than an ideal $Pm\bar{3}m$ perovskite represented by $a^0a^0a^0$ with Glazer notation (**Figure 1**a).[1] Focusing on the ubiquitous distortions, there have been symmetry arguments on macroscopic effects related to the octahedral rotations.[2–7] For example, a new type of symmetry operation termed a roto operation, which locally reverses the sense of the oxygen octahedral rotations, has been introduced to understand physical quantities coupled to the octahedral rotations such as rotomagnetism, in which magnetization is induced by octahedral rotations.[2] In addition, a path to design of ferroelectric (or multiferroic) materials by actively utilizing the oxygen octahedral rotations through a hybrid improper mechanism has been suggested.[3,4,6] In this mechanism, a polar distortion is induced by a combination of two kinds of octahedral rotations without introducing second-order Jahn–Teller active cations, i.e., lone-pair cations such as $Pb^{2+}$ and $d^0$ transition metal cations such as $Ti^{4+}$, to the A and B sites of perovskites, respectively.[6]

In addition to such symmetry arguments that predict the occurrence of as-yet-unestablished effects from a macroscopic viewpoint,[2–7] it is important in the material design to microscopically understand the origin and magnitude of the effects. Large rotomagnetic effects and robust multiferroic coupling through the hybrid improper mechanism are expected if magnetic interactions are induced and/or drastically changed by the octahedral rotations. What comes immediately to mind as a mechanism connecting magnetism to the octahedral rotations could be a superexchange interaction via an oxide ion[8,9] since their strength strongly depends on metal-oxygen-metal bond angles and hence the octahedral rotations. Materials whose magnetic interactions are intimately linked to the octahedral rotations via a novel mechanism are demanded to develop new functionalities such as the rotomagnetic effect.

Recently, we have presented first-principles calculations showing that antiferromagnetic (AFM) superexchange interactions via $M$ $n$d states play a predominant role in AFM ordering of $Eu^{2+}$ 4f spins ($S$ = 7/2) for divalent europium perovskites Eu$MO_3$ ($M$ = Ti, Zr, and Hf, and $n$ = 3, 4, and 5, respectively).[11] A strong spin-lattice coupling observed in $EuTiO_3$, including a large enhancement of the dielectric constant by a magnetic field[12] and ferromagnetism induced by a tensile strain,[13,14] a lattice expansion,[15–17] and an application of an electric field,[18] is explained by a competition between the AFM superexchange interaction via the Ti 3d states and ferromagnetic (FM) indirect exchange interaction via the Eu 5d states.[19,20] Since the $M$ $n$d states are strongly affected by the rotations of the $MO_6$ octahedra, the strength of superexchange interactions are expected to depend on the octahedral rotations.[21,22]

In this study, we perform systematic first-principles calculations on the magnetic interactions and electronic structure of the $Eu^{2+}$ perovskites for prototypal cubic ($Pm\bar{3}m$) and orthorhombic ($Pbnm$) models (Figure 1), the latter of which is represented by $a^-a^-c^+$ and experimentally observed for $EuZrO_3$ and $EuHfO_3$ at room temperature.[21] As a result, we find that the AFM superexchange interaction is strengthened by rotations of the $MO_6$ octahedra involved in the cubic to orthorhombic

Dr. H. Akamatsu, Dr. Y. Kumagai, Prof. F. Oba, Prof. I. Tanaka
Department of Materials Science and Engineering
Kyoto University
Sakyo, Kyoto, 606-8501, Japan
E-mail: hirofumi.akamatsu@gmail.com
Dr. Y. Kumagai
Department of Materials, ETH Zurich
Wolfgang-Pauli-Strasse, Zurich 8093, Switzerland
Prof. K. Fujita, Prof. K. Tanaka
Department of Material Chemistry
Kyoto University
Nishikyo, Kyoto 615-8510, Japan

DOI: 10.1002/adfm.201202477

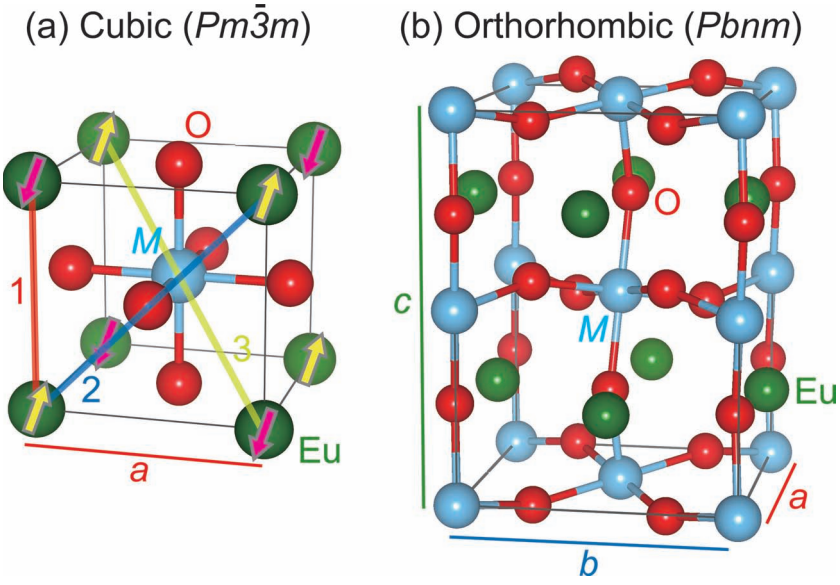


**Figure 1.** Schematics of a) cubic perovskite structure with space group $Pm\bar{3}m$ and b) orthorhombic structure with space group *Pbnm*. The arrows in (a) schematically indicate a *G*-type magnetic structure. The numbers 1, 2, and 3 denote the first, second, and third nearest-neighbor Eu-ion pairs, respectively. The crystal structures are visualized using VESTA code.[10]

structural change. Our calculations reveal that the magnetic ground state of $EuZrO_3$ and $EuHfO_3$ is changed from FM to AFM as their structure is varied from cubic to orthorhombic. An analysis of charge density shows that in $EuZrO_3$, overlap between the Eu 4f and Zr 4d states becomes larger with the structural change; the $ZrO_6$ octahedral rotations lower the site symmetry of $Zr^4$+, causing anisotropic development of the lobes of the 4d states of $Zr^4$+ toward the Eu sites. The enhancement of the superexchange interactions is explained based on a third-order perturbation. The superexchange interactions are strengthened due to the enhancement of the overlap integral between the Eu 4f and Zr 4d states as well as due to a decrease in energy gaps between the Eu 4f and Zr 4d states. Such enhancement of the AFM superexchange interactions occurs in $EuTiO_3$ and $EuHfO_3$ as well. Our results indicate that these perovskites possess a novel type of strong coupling between the magnetic properties and octahedral rotations.

## 2. Computational Methods

The calculations were performed using the projector augmented-wave (PAW) method[23] and the HSE06 hybrid functional[24–26] as implemented in the VASP code.[27–29] The HSE06 functional adopts the replacement of one-quarter of the exchange energy in the Perdew–Burke–Ernzerhof generalized gradient approximation (PBE-GGA)[30] with the nonlocal Fock exchange, and a screening parameter of 0.208 $Å^{-1}$. It has been shown that the hybrid Hartree–Fock density functional approach describes the electronic structure for a variety of molecules and solids more precisely than those obtained from the local and semilocal functional.[11,24–26,28,29,31–39] The calculation conditions have been described in detail in our previous reports.[11,21]

We mainly consider structural models possessing a space group of $Pm\bar{3}m$ and *Pbnm* with various cell volumes, which are referred to as cubic and orthorhombic models below, respectively. Cell shapes and internal coordinates were relaxed at any volume under the constraints of the symmetry of the unit cells. Tetragonal $\sqrt{2} \times \sqrt{2} \times 2$ supercells with four formula units were used for the cubic model in order to represent four magnetic configurations i.e., AFM *A*-, *C*-, *G*-, and FM *F*-types,[15,16] the total energies of which are necessary to estimate the first, second, and third nearest-neighbor (NN) exchange constants, $J_1$, $J_2$, and $J_3$, respectively, shown in Figure 1a. We confirmed that the ratio of the tetragonal lattice constants *a* to *c* approximately remained 1 to $\sqrt{2}$ at any volume. For the orthorhombic model, we use the unit cells illustrated in Figure 1b. The *A*-type ordering is assumed to have FM layers within the *ab* plane stacking antiferromagnetically along the *c* axis, and the *C*-type ordering has FM chains along the *c* axis that couple to the neighboring chains antiferromagnetically. $J_1$, $J_2$, and $J_3$ are defined as in the case of the cubic model by regarding the lattice composed of $Eu^{2+}$ ions as a simple cubic. Actually, there are three kinds of $J_1$, four kinds of $J_2$, and four kinds of $J_3$. In estimating the exchange constants by using total energies of the *A*- and *C*-types defined above, simply-averaged values are estimated for $J_1$ and $J_3$. However, estimated for $J_2$ are averaged values of the exchange constants between the second NN spins in the neighboring *ab* layers while the exchange constants between the second NN spins within the same *ab* layer are not included due to the model shape.

The first, second, and third NN exchange constants were calculated by mapping the total-energy difference between different magnetic configurations onto the Heisenberg spin Hamiltonian $H = -2\sum_{i>j} J^{ij} S_i \cdot S_j$, where $J^{ij}$ is the exchange constant of magnetic interactions between the Eu 4f spins at the *i* and *j* sites and $S_i$ is the spin vector at the *i* site.[11,13,15,16,21] The total energies per unit cell for *A*-, *C*-, *F*, and *G*-types, respectively, are represented by the exchange constants as follows:

$$E_A = E_0 + 2|S|^2(-4J_1 + 8J_2 + 16J_3) \quad (1)$$

$$E_C = E_0 + 2|S|^2(4J_1 + 8J_2 - 16J_3) \quad (2)$$

$$E_F = E_0 + 2|S|^2(-12J_1 - 24J_2 - 16J_3) \quad (3)$$

$$E_G = E_0 + 2|S|^2(12J_1 - 24J_2 + 16J_3) \quad (4)$$

where $|S|^2 = S(S+1)$ and $S = 7/2$ for $Eu^2$+. The values of $J_1$, $J_2$, and $J_3$ were obtained by substituting calculated total energies into the left-hand sides of Equation (1) to Equation (4) and then solving the simultaneous equations.

In order to estimate stabilization energies accompanied by structural distortions related to the $MO_6$ octahedral rotations,

the calculations were also performed for four other typical perovskite structures with different tilting patterns, i.e., *I4/mcm* ($a^0a^0c^-$), *P4/mbm* ($a^0a^0c^+$), *Ccmm* ($a^-b^0c^+$), and *Ibmm* ($a^-a^-c^0$) structures.[40] The cell parameters and atomic coordinates were relaxed under the constraints of the symmetry. As for $EuTiO_3$ with an *I4/mcm* structure, which is experimentally observed at low temperatures,[41–45] we calculated total-energy differences between *G*- and *F*-type magnetic configurations as a function of cell volume for comparison with experiments. This structural model is denoted as a tetragonal model below.

## 3. Results and Discussion

We begin with reviewing fundamental properties of the $Eu^{2+}$ perovskites including structural, magnetic, and optical properties investigated experimentally and theoretically so far. $EuTiO_3$ has a cubic $Pm\bar{3}m$ structure at room temperature, while $EuZrO_3$ and $EuHfO_3$ have orthorhombic *Pbnm* structures.[12,21,46–48] As for $EuTiO_3$, the occurrence of antiferrodistortive transition from cubic $Pm\bar{3}m$ to tetragonal *I4/mcm* structure has been recently indicated by a specific heat measurement,[41] variable-temperature powder X-ray diffraction,[42,43] electron diffraction,[43] and first-principles calculations.[44,45] The lattice constants are well reproduced by the calculations.[21] We compare in **Figure 2** the total energies of $EuMO_3$ (*M* = Ti, Zr, and Hf) with different octahedral tilting patterns to that of the cubic $Pm\bar{3}m$ structure taken as a reference.[40] For $EuZrO_3$ and $EuHfO_3$, the lowest energy is obtained for the *Pbnm* structure in agreement with the experimental results. On the other hand, for $EuTiO_3$, the structures with *I4/mcm* and *Ibmm* symmetry are more stable than the $Pm\bar{3}m$ structure, and they are nearly degenerate. The *P4/mbm*, *Ccmm*, and *Pbnm* structures relax to the $Pm\bar{3}m$, *I4/mcm*, and *Ibmm* structures, respectively. These results agree well with the recent results of GGA+*U* calculations.[45] Hereinafter, we refer *Ibmm* structure for $EuTiO_3$ and *Pbnm* structure for $EuZrO_3$ and $EuHfO_3$ as orthorhombic structures for simplicity.

The optical band gaps are estimated to be 0.8, 2.4, and 2.7 eV for $EuTiO_3$, $EuZrO_3$, and $EuHfO_3$, respectively, from diffuse reflectance spectra measured at room temperature.[21] **Figure 3** shows site-projected density of states (DOS) of the perovskites for both cubic and orthorhombic models. Band gaps, $E_g$, which are also shown in Figure 3, are in good agreement with the experimental optical band gaps. The highest occupied bands are mainly composed of Eu 4f states, and have a narrow width, indicating the localized nature of the Eu 4f electrons. It should be noted that *M* nd components (*M* = Ti, Zr, and Hf and *n* = 3, 4, and 5, respectively) as well as O 2p components are also observed in the energy region of the Eu 4f bands. The O 2p bands lie below the Eu 4f bands. The lowest unoccupied bands, on the other hand, chiefly consists of the *M* *n*d states. The Eu 5d states form broad bands that are located above the *M* *n*d states.

Paramagnetic to AFM transitions are observed at $T_N$ = 5.5, 4.1, and 3.9 K for $EuTiO_3$, $EuZrO_3$, and $EuHfO_3$, respectively. Powder neutron diffraction study indicates that $EuTiO_3$ has a *G*-type magnetic configuration below $T_N$.[49] Negative values of $J_1$ and positive values of $J_2$ are derived from Weiss temperature, $\theta_W$, and Néel temperature, $T_N$, based on the molecular-field theory.[12,21,47,48] For tetragonal $EuTiO_3$ and orthorhombic $EuZrO_3$ and $EuHfO_3$ as well as cubic $EuTiO_3$, the calculated total-energy differences between *G*- and *F*-type magnetic configurations, $E_G$–$E_F$ [$=2|\mathbf{S}|^2(24J_1+32J_3)$], which correspond to an inter-sublattice interaction in the *G*-type AFM configuration (see the arrows in Figure 1a), are plotted as a function of cell volume in **Figure 4**a. The calculations reproduce AFM ground states for the perovskites at their equilibrium cell volumes. The energy difference can be experimentally derived from $\theta_W$ and $T_N$ as $E_G$–$E_F = 6k_B(\theta_W - T_N)$ since according to the molecular-field theory, $\theta_W = 2|\mathbf{S}|^2/3k_B(6J_1+12J_2+8J_3)$ and $T_N = 2|\mathbf{S}|^2/3k_B(-6J_1+12J_2-8J_3)$ within the third NN interactions. The experimental values are also plotted in Figure 4a against the experimental cell volumes. These values are well reproduced by the calculations. An increase in cell volume leads to switching of the magnetic ground state from AFM to FM for both cubic and tetragonal $EuTiO_3$, which is in good agreement with the experimental results that FM behavior is observed for epitaxial $EuTiO_3$ thin films with a *c*-axis elongation[17] and a biaxial tensile strain.[14] This behavior is interpreted in terms

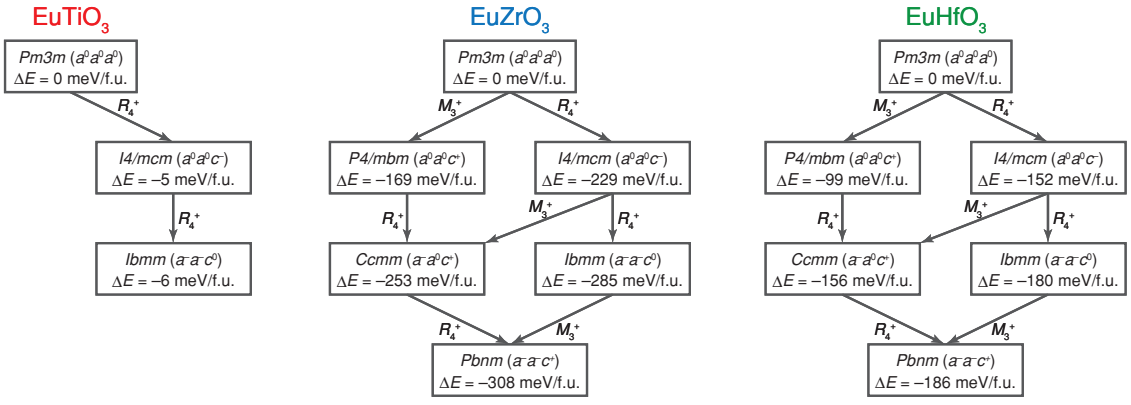


**Figure 2.** Total energies of $EuMO_3$ (*M* = Ti, Zr, and Hf) with different octahedral tilting patterns relative to the energy of the cubic $Pm\bar{3}m$ ($a^0a^0a^0$) structure for the *G*-type magnetic configuration. The types of additional octahedral rotations are denoted by $M^+_3$ (in phase) and $R^+_4$ (out of phase).

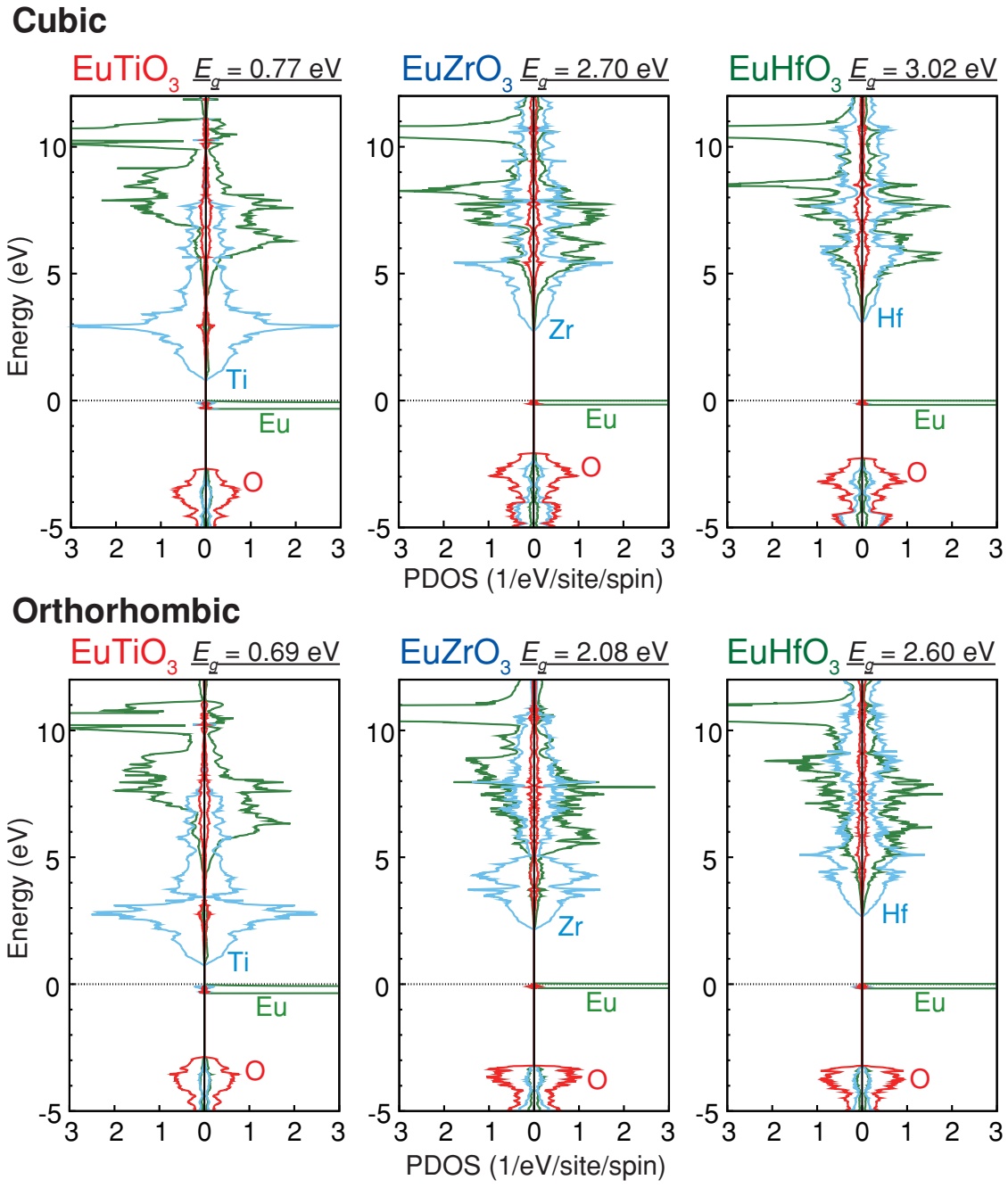


**Figure 3.** Site-projected density of states for Eu$MO_3$ [$M$ = Ti (left), Zr (center), and Hf (right)] in cubic (top) and orthorhombic (bottom) models. The $G$-type magnetic configurations are adopted. The zero energies are set to the highest occupied states. Band gaps ($E_g$) estimated as a difference between the eigenvalues for the lowest unoccupied and highest occupied states are also shown.

of competition between the AFM superexchange interactions via the Ti 3d states and the FM indirect exchange interactions via the Eu 5d states in the inter-sublattice interaction.[11] In orthorhombic $EuZrO_3$ and $EuHfO_3$, the AFM superexchange interactions via the Zr 4d and Hf 5d states, respectively, are so stronger than the FM exchange interaction in the calculated volume range that no sign reversal of $J_1$ occurs and $J_1$ decreases monotonously with a decrease in cell volume. Figure 4a also shows the cell-volume dependence of $E_G$–$E_F$ for as-yet-unsynthesized cubic $EuSiO_3$ for comparison. It has a negative slope against cell volume in sharp contrast to the above three perovskites because the FM exchange interaction is predominant for Si due to the absence of d states that mediate the AFM superexchange interactions.[11] A charge-density difference between two compounds is helpful in understanding the difference in their chemical bonding.[39] The charge-density

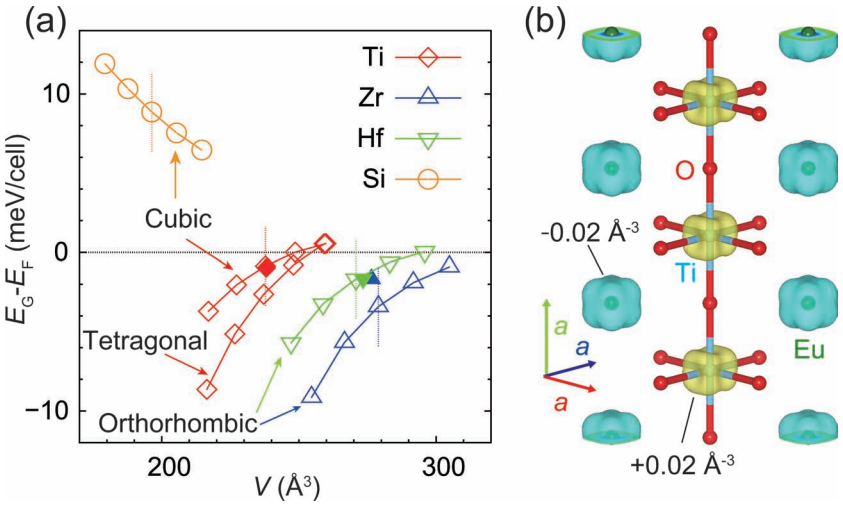


**Figure 4.** a) Cell-volume dependence of the total-energy difference between *G*-type antiferromagnetic and ferromagnetic states for $EuTiO_3$ for the cubic and tetragonal (*I*4/*mcm*) models, Eu*MO*$_3$ with *M* = Zr and Hf for the orthorhombic models, and $EuSiO_3$ for the cubic model. The broken vertical lines indicate the equilibrium volumes. The energy differences estimated experimentally are plotted against the experimental cell volume as indicated by the filled marks.[21] b) Difference in charge density integrated within the energy region of Eu 4f bands between cubic $EuTiO_3$ and $EuSiO_3$. The structure with the averaged lattice constant between two optimized cubic structure was used. The yellow (+0.02 Å$^{-3}$) and blue (–0.02 Å$^{-3}$) isosurface means excess and deficiency of charge in $EuTiO_3$ relative to $EuSiO_3$. The crystal structures and isosurfaces are visualized using VESTA code.[10]

difference for the Eu 4f bands between cubic $EuTiO_3$ and $EuSiO_3$ are depicted in Figure 4b. The charge density around the Eu and Ti sites is decreased and increased, respectively, in $EuTiO_3$ when compared to $EuSiO_3$ while that around the O sites is similar. This result supports the significance of contribution of Ti 3d states in the Eu 4f bands. This is also seen in the site-projected DOS shown in Figure 3 as a mixing of the Ti 3d states in the Eu 4f bands.

Thus, the calculations well reproduce the fundamental properties such as lattice constants, band gaps, and magnetic structures observed experimentally. However, if the relationship between the electronic structure and exchange constants across the perovskites is carefully considered, we face seemingly puzzling behavior. According to an analysis based on the molecular-orbital theory, the superexchange interactions between the Eu 4f spins via the *M nd* states are approximately represented as a third-order perturbation from an atomic orbital basis as follows:

$$J_{SE} \propto \frac{\sigma_{df}^4}{(\Delta E)^2} \quad (5)$$

where $\sigma_{df}$ and $\Delta E$ are an overlap integral and an energy gap between the Eu 4f and *M nd* orbitals.[50] This equation indicates that the AFM superexchange interaction becomes weaker rapidly with an increase in $\Delta E$ if $\sigma_{df}$ is constant. $E_g$ approximately corresponds to $\Delta E$. The site-projected DOS shown in Figure 3 shows that $E_g$ increases from cubic $EuTiO_3$ to orthorhombic $EuZrO_3$ and $EuHfO_3$. However, the AFM interactions between the sublattices are, in fact, stronger in orthorhombic $EuZrO_3$ and $EuHfO_3$ than in cubic $EuTiO_3$ (see Figure 4a), in contrast to a trend expected from Equation (5) in terms of $\Delta E$. This implies that another factor than $\Delta E$, i.e., $\sigma_{df}$, could be significantly varied between the cubic and orthorhombic structures. It should be also noted that the AFM inter-sublattice interactions are significantly stronger for tetragonal $EuTiO_3$ than for cubic $EuTiO_3$ although $E_g$ is almost the same for the both models ($E_g$ = 0.73 eV for tetragonal $EuTiO_3$; data is not shown), implying that the small octahedral-rotation angle around the *c* axis (6.35°) in the tetragonal model brings about the enhancement of the interactions, probably, due to an increase in $\sigma_{df}$. Therefore, we concentrate on discussion of the difference in the magnetic interactions and electronic structure between the cubic and orthorhombic models below.

The calculated values of $J_1$, $J_2$, and $J_3$ are plotted in **Figure 5** as a function of cell volume for the perovskites with the cubic and orthorhombic models. The magnitude of $J_3$ is much smaller than those of $J_1$ and $J_2$ for any perovskites with any structural models. Therefore, the cell-volume dependence of $J_1$ is similar to that of $E_G$–$E_F$ [= $2|\mathbf{S}|^2(24J_1 + 32J_3)$] shown in Figure 4a for cubic $EuTiO_3$ and orthorhombic $EuZrO_3$ and $EuHfO_3$. Interestingly, $EuZrO_3$ and $EuHfO_3$ with the cubic models show positive values of $J_1$ and hence the FM ground state in the whole volume range in sharp contrast to the case of the orthorhombic models, while $J_2$ is almost independent of the structural models. In addition, the slopes of $J_1$ against cell volume are negative for the cubic model contrary to those for the orthorhombic model. The behavior of $J_1$ for the cubic models across the perovskites can be explained in terms of $\Delta E$; the AFM superexchange interactions are much weaker for $EuZrO_3$ and $EuHfO_3$ than for $EuTiO_3$ due to the larger $\Delta E$ if $\sigma_{df}$ is almost same. For any perovskites, changing from cubic to orthorhombic, $J_1$ decreases significantly, indicating that the orthorhombic *Pbnm* structures with the $MO_6$ octahedral rotations favor the AFM coupling between the first NN Eu 4f spins compared to the cubic $Pm\bar{3}m$ structures.

**Figures 6**a,b illustrate the $MO_6$ octahedral rotation patterns in the orthorhombic *Pbnm* structure ($a^-a^-c^+$). Here, the two rotation angles, $\theta^{a-}$ and $\theta^{c+}$, are defined as shown in Figures 6a,b. For orthorhombic $EuZrO_3$ and $EuHfO_3$ at the equilibrium volume, ($\theta^{a-}$, $\theta^{c+}$) are (9.2°, 8.4°) and (8.2°, 7.4°), respectively. These values are slightly larger than the experimental values obtained from synchrotron X-ray diffraction at room temperature, i.e., (7.13°, 6.64°) and (7.18°, 5.60°) for $EuZrO_3$ and $EuHfO_3$, respectively.[21] Both $\theta^{a-}$ and $\theta^{c+}$ increase with a decrease in cell volume. Such octahedral rotations could enhance the AFM superexchange interaction. As mentioned above, the *Pbnm* structure is unstable and relaxes to *Ibmm* structure ($a^-a^-c^0$) for $EuTiO_3$. $\theta^{a-}$ becomes larger as cell volume decreases, while $\theta^{c+}$ is zero within the numerical error. Although the rotation angles are smaller in $EuTiO_3$ than those in $EuZrO_3$ and $EuHfO_3$, the AFM superexchange interaction is significantly enhanced as shown in Figure 5.

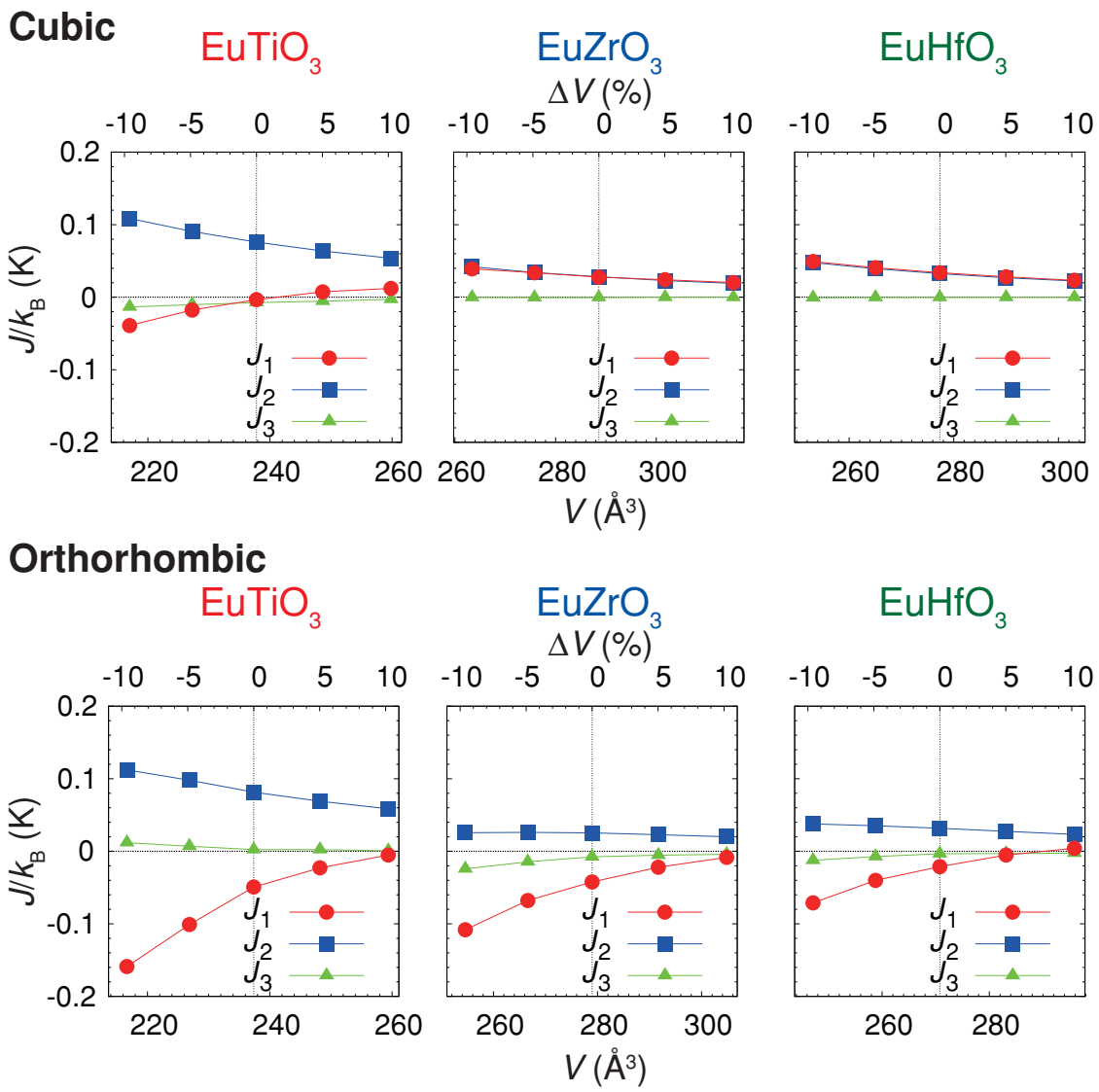


**Figure 5.** Cell-volume dependence of $J_1$, $J_2$, and $J_3$ for Eu$MO_3$ [$M$ = Ti (left), Zr (center), and Hf (right)] with cubic (top) and orthorhombic (bottom) models. $\Delta V = 0$ indicates the equilibrium volume. Positive and negative values indicate FM and AFM interactions, respectively.

We now discuss the microscopic origin of the enhancement of the AFM interactions by the octahedral rotations. As seen in Equation (5), the important factors in the AFM superexchange interactions are an energy gap ($\Delta E$) and an overlap integral ($\sigma_{df}$) between the Eu 4f and $M$ nd orbitals. The site-projected DOS and $E_g$ values are shown for the perovskites with the cubic and orthorhombic models in Figure 3. Within the cubic models, the fact that $J_1$ is much lower in $EuTiO_3$ than in $EuZrO_3$ and $EuHfO_3$ can be interpreted in terms of the difference in $\Delta E$, as mentioned above. The $E_g$ values decrease by at most 25% when the structures are changed from cubic to orthorhombic. When one compares each compound with cubic and orthorhombic structures, the enhancement of the AFM superexchange interactions accompanied by the structural change seems to be difficult to explain only in terms of such small decreases in $\Delta E$, in particular, for $EuZrO_3$ and $EuHfO_3$. In addition, when comparing orthorhombic $EuTiO_3$ and $EuZrO_3$, $J_1$ is similar to each other at the equilibrium volume while $E_g$ is much larger for $EuZrO_3$ (2.10 eV) than that for $EuTiO_3$ (0.69 eV). These facts suggest the importance of another factor for the AFM superexchange interaction, i.e., $\sigma_{df}$. Therefore, it is necessary to consider a difference in the overlap of the $M$ d orbitals with the Eu 4f orbitals between the cubic and orthorhombic structures to understand the enhancement of the AFM interactions by the octahedral rotations.

To focus on the overlap between the Eu 4f and $M$ d orbitals, charge-density isosurfaces of the Eu 4f bands are illustrated as a function of cell volume for cubic $EuTiO_3$ and cubic and orthorhombic $EuZrO_3$ in **Figure 7**. For cubic $EuTiO_3$ (Figure 7a), a non-negligible amount of charge density is recognized around the Ti and O sites as well as the Eu sites, indicating a hybridization of the Eu 4f states with the Ti 3d and O 2p states.

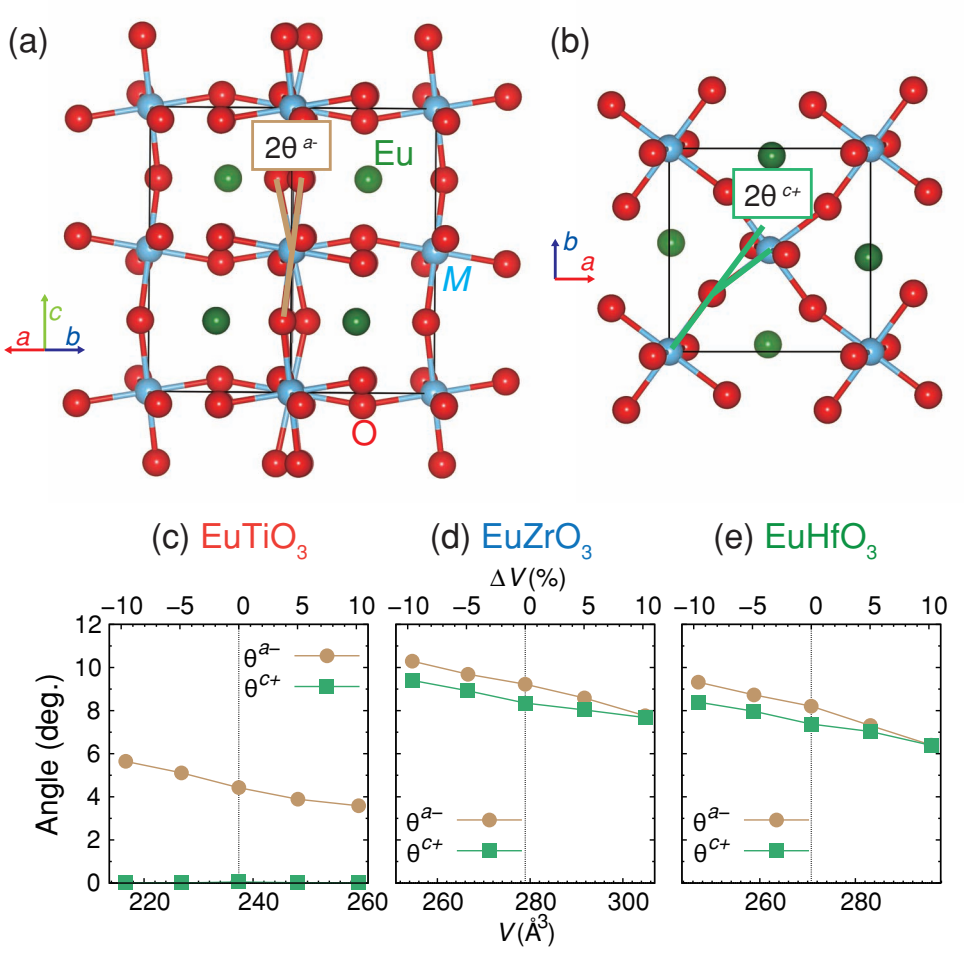


**Figure 6.** Schematics of $MO_6$ octahedral rotations along the direction a) perpendicular to and b) parallel to the *c* axis in an orthorhombic *Pbnm* structure ($a^-a^-c^+$). The rotation angles $\theta^{a-}$ and $\theta^{c+}$ are defined in (a) and (b), respectively. Cell-volume dependence of $\theta^{a-}$ and $\theta^{c+}$ for orthorhombic Eu$MO_3$ for $M$ = c) Ti, d) Zr, and e) Hf with *G*-type magnetic configurations. $\Delta V = 0$ indicates the equilibrium volume.

The charge density around the Ti sites reflects its site symmetry ($m\bar{3}m$), and thereby the Ti 3d orbitals overlap equally with the Eu 4f orbitals at the eight equivalent Eu sites. A decrease in cell volume leads to an increase in the charge density around the Ti sites, indicating the enhancement of the hybridization of the Eu 4f and Ti 3d states and hence the AFM superexchange interaction via the Ti 3d states. This result corresponds to a decrease in $J_1$ with lowering cell volume (see Figure 5). On the other hand, no charge-density isosurfaces around the Zr sites are recognized for cubic $EuZrO_3$ with any cell volume. This indicates that the hybridization between the Eu 4f and *M* d states is much weaker in cubic $EuZrO_3$ than in cubic $EuTiO_3$. Therefore, the AFM superexchange interaction via the Zr 4d states is overwhelmed by the competing FM exchange interaction via the Eu 5d states for $J_1$ in cubic $EuZrO_3$, resulting in the FM ground states. In the case of orthorhombic $EuZrO_3$, one can see anisotropic development of charge density around the Zr ions with site symmetry of $\bar{1}$. The lowering of site symmetry accompanied by the $a^-a^-c^+$ octahedral rotations allows the anisotropic spreading of the Zr 4d orbital. This clearly corroborates that the AFM superexchange interaction via the Zr 4d states is enhanced in orthorhombic $EuZrO_3$ as compared to cubic $EuZrO_3$. It should be noted that although the lobes of the Zr 4d orbitals extend, in particular, toward the two Eu ions that are the nearest to the Zr ions, the distance between the Eu and Zr ions is not the most crucial factor for the AFM superexchange interaction; we have confirmed that a considerable amount of charge density is discerned around the Zr sites in orthorhombic $EuZrO_3$ with $\Delta V$ = +9.3% but not in cubic $EuZrO_3$ with $\Delta V$ = –8.7%, in which the equivalent Eu-Zr distance is smaller than the smallest Eu-Zr distance in the former (data not shown). The site-symmetry lowering by the octahedral rotations is the most essential factor for the enhancement of the interaction between the Eu 4f and Zr 4d states.

## 4. Conclusions

Using first-principles calculations, we have investigated the electronic structure, magnetism, and their relationship for Eu$MO_3$ ($M$ = Ti, Zr, and Hf) with the cubic $Pm\bar{3}m$ and orthorhombic *Pbnm* models. The $MO_6$ octahedral rotations accompanied by

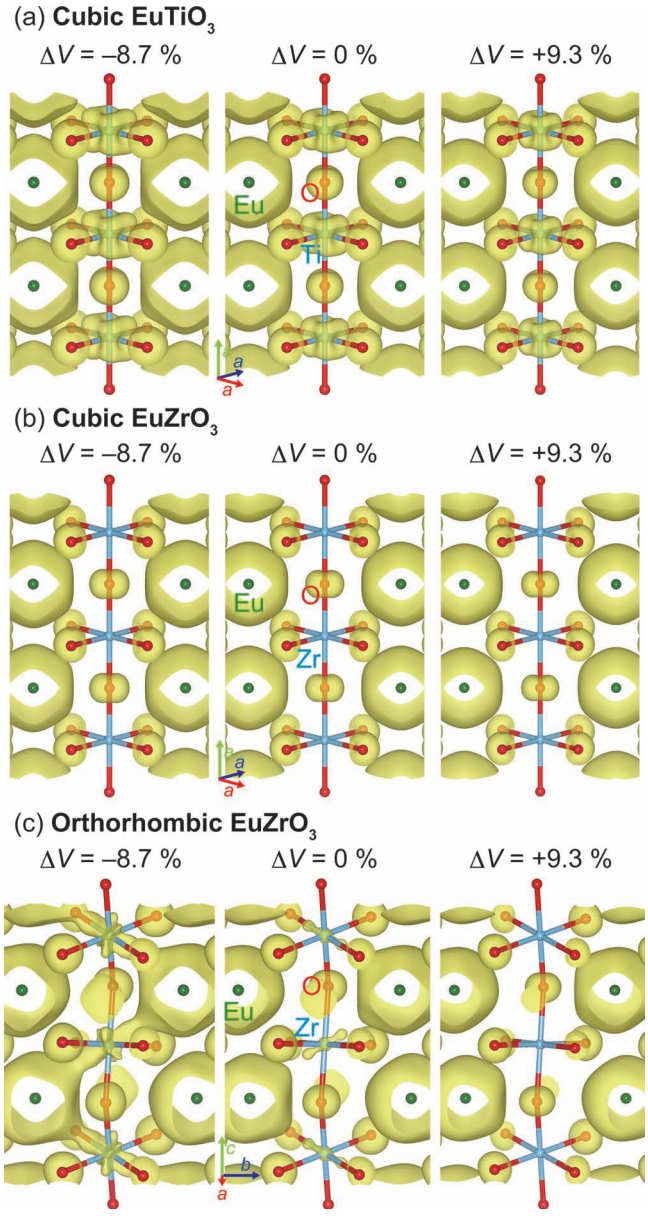


**Figure 7.** Cell-volume dependence of isosurfaces of charge density integrated within the energy region of the Eu 4*f* bands for *G*-type a) cubic $EuTiO_3$ and b) cubic and c) orthorhombic $EuZrO_3$. The isosurfaces are depicted at 0.005 $Å^{-3}$.

the structural change from cubic to orthorhombic lead to the drastic enhancement of the AFM superexchange interactions between the Eu 4f spins via the *M* n*d* states (*M* = Ti, Zr, and Hf, and *n* = 3, 4, and 5). The octahedral rotations not only reduce energy gaps between the Eu 4f and *M* n*d* states but also facilitate a spatial overlap between the Eu 4f and *M* d orbitals. One of the remarkable results is that the octahedral rotations alter the magnetic ground states for $EuZrO_3$ and $EuHfO_3$: the magnetic ground state is switched from FM into AFM when the structure is changed from cubic to orthorhombic. In other words, the octahedral rotations are indispensable for AFM ordering of the Eu 4f spins observed experimentally in $EuZrO_3$ and $EuHfO_3$. Thus, the present results reveal that these perovskites belong to a class of materials exhibiting a novel type of strong correlation between their magnetism and octahedral rotations. In closing, although investigations on strain effects are outside of the scope of this paper, the magnetic and dielectric properties of $EuZrO_3$ and $EuHfO_3$ epitaxial thin films are very fascinating in that they could be multiferroic (FM and ferroelectric) as with $EuTiO_3$,[13] by using strain engineering so as to suppress the octahedral rotations and induce a polar distortion.[7,40,51,52]

## Acknowledgements

This research was supported by Grants-in-Aid for Scientific Research (B) (No. 22360273), Challenging Exploratory Research (No. 23655198), and Young Scientists (A) (No. 23686089) from MEXT and for JSPS Fellows (No. 22-1280) and JSPS Fellows for Research Abroad (No. 23-470) from JSPS. This article was modified after online publication. The affiliation for Prof. K. Tanaka was corrected.

Received: August 28, 2012
Published online: November 19, 2012

[1] A. M. Glazer, *Acta Crystallogr.* **1972**, *B 28*, 3384.
[2] V. Gopalan, D. B. Litvin, *Nat. Mater.* **2011**, *10*, 376.
[3] E. Bousquet, M. Dawber, N. Stucki, C. Lichtensteiger, P. Hermet, S. Gariglio, J.-M. Triscone, P. Ghosez, *Nature* **2008**, *452*, 732.
[4] N. A. Benedek, C. J. Fennie, *Phys. Rev. Lett.* **2011**, *106*, 107204.
[5] J. M. Rondinelli, N. A. Spaldin, *Adv. Mater.* **2011**, *23*, 3363.
[6] J. M. Rondinelli, C. J. Fennie, *Adv. Mater.* **2012**, *24*, 1961.
[7] E. Bousquet, N. Spaldin, *Phys. Rev. Lett.* **2011**, *107*, 197603.
[8] J. Kanamori, *J. Phys. Chem. Solids* **1959**, *10*, 87.
[9] J. B. Goodenough, *Phys. Rev.* **1955**, *100*, 564.
[10] K. Momma, F. Izumi, *J. Appl. Crystallogr.* **2008**, *41*, 653.
[11] H. Akamatsu, Y. Kumagai, F. Oba, K. Fujita, H. Murakami, K. Tanaka, I. Tanaka, *Phys. Rev. B* **2011**, *83*, 214421.
[12] T. Katsufuji, H. Takagi, *Phys. Rev. B* **2001**, *64*, 054415.
[13] C. J. Fennie, K. M. Rabe, *Phys. Rev. Lett.* **2006**, *97*, 267602.
[14] J. H. Lee, L. Fang, E. Vlahos, X. Ke, Y. W. Jung, L. F. Kourkoutis, J.-W. Kim, P. J. Ryan, T. Heeg, M. Roeckerath, V. Goian, M. Bernhagen, R. Uecker, P. C. Hammel, K. M. Rabe, S. Kamba, J. Schubert, J. W. Freeland, D. A. Muller, C. J. Fennie, P. Schiffer, V. Gopalan, E. J. Halperin, D. G. Schlom, *Nature* **2010**, *466*, 954.
[15] R. Ranjan, H. S. Nabi, R. Pentcheva, *J. Phys.: Condens. Matter* **2007**, *19*, 406217.
[16] R. Ranjan, H. S. Nabi, R. Pentcheva, *J. Appl. Phys.* **2009**, *105*, 053905.
[17] K. Fujita, N. Wakasugi, S. Murai, Y. Zong, K. Tanaka, *Appl. Phys. Lett.* **2009**, *94*, 062512.
[18] P. J. Ryan, J.-W. Kim, T. Birol, P. Thompson, J.-H. Lee, X. Ke, P. S. Normile, E. Karapetrova, P. Schier, S. D. Brown, C. J. Fennie, D. G. Schlom, *ArXiv e-Print Arch.* **2012**, *1206*, 5181.
[19] J. B. Goodenough, *Magnetism and the Chemical Bond*, Interscience, New York **1963**.
[20] T. Kasuya, *IBM J. Res. Dev.* **1970**, *14*, 214.
[21] H. Akamatsu, K. Fujita, H. Hayashi, T. Kawamoto, Y. Kumagai, Y. Zong, K. Iwata, F. Oba, I. Tanaka, K. Tanaka, *Inorg. Chem.* **2012**, *51*, 4560.
[22] T. Birol, N. A. Benedek, H. Das, A. L. Wysocki, A. T. Mulder, B. M. Abbett, E. H. Smith, S. Ghosh, C. J. Fennie, *ArXiv e-Print Arch.* **2012**, *1207*, 5026.
[23] P. E. Blöchl, *Phys. Rev. B* **1994**, *50*, 17953.

[24] J. Heyd, G. E. Scuseria, M. Ernzerhof, *J. Chem. Phys.* **2003**, *118*, 8207.
[25] J. Heyd, G. E. Scuseria, M. Ernzerhof, *J. Chem. Phys.* **2006**, *124*, 219906.
[26] A. V. Krukau, O. A. Vydrov, A. F. Izmaylov, G. E. Scuseria, *J. Chem. Phys.* **2006**, *125*, 224106.
[27] G. Kresse, D. Joubert, *Phys. Rev. B* **1999**, *59*, 1758.
[28] J. Paier, M. Marsman, K. Hummer, G. Kresse, I. C. Gerber, J. G. Angyan, *J. Chem. Phys.* **2006**, *124*, 154709.
[29] J. Paier, M. Marsman, K. Hummer, G. Kresse, I. C. Gerber, J. G. Angyan, *J. Chem. Phys.* **2006**, *125*, 249901.
[30] J. P. Perdew, K. Burke, M. Ernzerhof, *Phys. Rev. Lett.* **1996**, *77*, 3865.
[31] K. N. Kudin, G. E. Scuseria, R. L. Martin, *Phys. Rev. Lett.* **2002**, *89*, 266402.
[32] C. Franchini, V. Bayer, R. Podloucky, J. Paier, G. Kresse, *Phys. Rev. B* **2005**, *72*, 045132.
[33] F. Oba, A. Togo, I. Tanaka, J. Paier, G. Kresse, *Phys. Rev. B* **2008**, *77*, 245202.
[34] F. Oba, A. Togo, I. Tanaka, K. Watanabe, T. Taniguchi, *Phys. Rev. B* **2010**, *81*, 075125.
[35] A. Stroppa, M. Marsman, G. Kresse, S. Picozzi, *New J. Phys.* **2010**, *12*, 093026.
[36] M. Choi, F. Oba, I. Tanaka, *Phys. Rev. B* **2011**, *83*, 214107.
[37] M. Choi, F. Oba, I. Tanaka, *Appl. Phys. Lett.* **2011**, *98*, 172901.
[38] Y. Kumagai, Y. Soda, F. Oba, A. Seko, I. Tanaka, *Phys. Rev. B* **2012**, *85*, 033203.
[39] Y. Kumagai, A. A. Belik, M. Lilienblum, N. Leo, M. Fiebig, N. A. Spaldin, *Phys. Rev. B* **2012**, *85*, 174422.
[40] S. Amisi, E. Bousquet, K. Katcho, P. Ghosez, *Phys. Rev. B* **2012**, *85*, 064112.
[41] A. Bussmann-Holder, J. Köhler, R. K. Kremer, J. M. Law, *Phys. Rev. B* **2011**, *83*, 212102.
[42] M. Allieta, M. Scavini, L. J. Spalek, V. Scagnoli, H. C. Walker, C. Panagopoulos, S. S. Saxena, T. Katsufuji, C. Mazzoli, *Phys. Rev. B* **2012**, *85*, 184107.
[43] V. Goian, S. Kamba, O. Pacherova, J. Drahokoupil, L. Palatinus, M. Dusek, J. Rohlicek, F. Laufek, W. Schranz, A. Fuith, M. Kachlik, K. Maca, A. Shkabko, L. Sagarna, A. Weidenkaff, A. A. Belik, *Phys. Rev. B* **2012**, *86*, 054112.
[44] J. L. Bettis, M.-H. Whangbo, J. Köhler, A. Bussmann-Holder, A. R. Bishop, *Phys. Rev. B* **2011**, *84*, 184114.
[45] K. Z. Rushchanskii, N. A. Spaldin, M. Lĕzaíc, *Phys. Rev. B* **2012**, *85*, 104109.
[46] J. Brous, I. Fankuchen, E. Banks, *Acta Crystallogr.* **1953**, *6*, 67.
[47] V. Viallet, J.-F. Marucco, J. Saint, M. Herbst-Ghysel, N. Dragoe, *J. Alloys Compd.* **2008**, *461*, 346.
[48] Y. Zong, K. Fujita, H. Akamatsu, S. Murai, K. Tanaka, *J. Solid State Chem.* **2010**, *183*, 168.
[49] T. R. McGuire, M. W. Shafer, R. J. Joenk, H. A. Alperin, S. J. Pickart, *J. Appl. Phys.* **1966**, *37*, 981.
[50] G. F. Dionne, *Magnetic Oxides*, Springer, New York **2009**.
[51] S. Bhattacharjee, E. Bousquet, P. Ghosez, *Phys. Rev. Lett.* **2009**, *102*, 117602.
[52] Y. Gu, K. Rabe, E. Bousquet, V. Gopalan, L.-Q. Chen, *Phys. Rev. B* **2012**, *85*, 064117.